Advances in Materials Research, *Vol. 14, No. 6 (2025) 467-491*
https://doi.org/10.12989/amr.2025.14.6.467

Machine learning (ML) method for static response estimation of FG plates using the novel 3D functions based on Shear-locking free meshless method

Seyed A. Vakili[1a], Farzad Shahabian[*1] and Mohammad H. GhadiriRad[2b]

[1]*Civil Engineering Department, Faculty of Engineering, Ferdowsi University of Mashhad, Iran*
[2]*Department of Civil Engineering, Faculty of Engineering Science, Quchan University of Technology, Iran*

(*Received December 3, 2024, Revised November 3, 2025, Accepted November 24, 2025*)

Abstract. This paper analyzes the static response of power-law thick functionally graded plates (P-FGPs) using the refined Element-Free Galerkin (EFG) method. The C1 continuity requirements of the displacement field are accurately and effectively fulfilled. A method is also presented that eliminates the shear-locking phenomenon through the use of specific shape functions. The stretching effect is approximated using higher order shear deformation theory (HSDT), and the shear correction factor is not required. According to Reddy's power law rule of mixture, the Young's modulus and Poisson's ratio of the two-phase metal–ceramic membrane vary continuously through the thickness. Furthermore, a three-dimensional function based on machine learning is employed to estimate the central deflection. This study introduces a novel three-dimensional estimating function for the central deflection of FGPs based on the results of the EFG method and sigmoid-cubic functions, representing the first application of this approach in the literature. Comparison with existing results demonstrates that the proposed estimation function provides an excellent fit to the response curve and is highly efficient for analyzing the static bending behavior of thick FGPs.

Keywords: bending; deformation theory; Element-Free Galerkin; higher order shear estimation function; power law functionally graded plates

1. Introduction

Functionally graded materials (FGMs) represent an advanced class of composites initially developed by Japanese researchers in 1984 for spacecraft thermal protection systems (Slimani *et al*. 2024, Amiri *et al*. 2020). These materials possess a continuously varying microstructure in which the volume fractions of metal and ceramic phases change smoothly along a specified direction, resulting in spatially dependent mechanical properties (Ghadiri Rad *et al*. 2015). Such gradation enables superior stiffness-to-weight ratios and enhanced structural performance. For accurate modeling of FGMs, numerical formulations must capture the continuous variation of material properties (Singh *et al*. 2024, Taczała *et al*. 2022). Among the available approaches, the rule of

*Corresponding author, Professor, E-mail: shahabf@um.ac.ir
[a] Ph.D. Student, E-mail: aminvakili@mail.um.ac.ir
[b] Ph.D., E-mail: Hosein_ghadiri@qiet.ac.ir

http://www.techno-press.org/?journal=amr&subpage=5 ISSN: 2234-0912 (Print), 2234-179X (Online)

mixtures (Vakili *et al*. 2019, Thang *et al*. 2023), Mori-Tanka (Vel *et al*. 2002) and Halpin-Tsai (Rad *et al*. 2020) methods are commonly employed to model the material gradation characteristics of FGMs.

A notable subclass of FGMs is the functionally graded plate (FGP), in which material properties vary continuously along the thickness direction. FGP overcome delamination and interfacial separation issues commonly found in laminated plates. Owing to their superior mechanical efficiency and adaptability, FGPs have found widespread application in aerospace, mechanical, and civil engineering fields (Keleshteri *et al*. 2022, Khalfi *et al*. 2024). In recent years, numerous studies have focused on the static, free vibration, dynamic, and buckling analyses of FG plates. For instance, Chakraborty (2003) proposed a finite element model for the bending analysis of FGPs using the third shear deformation theory. Swami *et al*. (2021) proposed an analytical solution based on a higher-order shear deformation theory for the analysis of thick multilayer plates subjected to thermal loading. Mudhafer *et al*. (2021) investigated the bending characteristics of ceramic-metal FGPs on the elastic foundation under the effect of moisture and thermal loading. Li *et al*. (2023, 2024) investigated the bending behavior of FGPs using the four variable plate theory. Slimani *et al*. (2024) proposed a novel quasi-3D approach based on higher-order shear deformation theory (HSDT) for the flexural analysis of porous FGPs, considering the thickness stretching effect. Benmalek *et al*. (2024) employed a mixed finite element formulation based on the Euler–Bernoulli and Timoshenko beam theories for bending analysis of FGPs. Houari *et al*. (2024) performed a thermoelastic flexural analysis of FG sandwich plates with symmetric and asymmetric FGM cores using a novel integrated HSDT. Van Vinh *et al*. (2023) analyzed the static bending behavior of FGPs based on HSDT principles, utilizing a four-node element (MiQ4) for numerical implementation. Multi-objective optimization for free vibration of L-shaped bi-functionally graded sandwich plates using an effective finite element method and non-dominated sorting genetic algorithm was carried out by Pham *et al*. (2023). Belarbi *et al*. (2024) examined the bending response of FG sandwich plates under combined thermal and mechanical loads, adopting an exponential–cubic–sinusoidal integral shear deformation theory.

Several theories have been developed to analyze plate structures. The Classical Plate Theory (CPT) is the earliest formulation, which neglects transverse shear deformations. However, in thick plates, these deformations cannot be ignored, making CPT unsuitable and leading to significant errors. To address this, the First-Order Shear Deformation Theory (FSDT) was introduced, which accounts for shear effects (Zenkur *et al*. 2012). Nevertheless, this theory requires the use of a shear correction factor to satisfy the zero transverse shear stress conditions on the upper and lower surfaces of the plate. It should be noted that determining this correction factor for plates made of functionally graded materials (FGMs) is quite challenging. Therefore, the Third-Order Shear Deformation Theory (TSDT) has been proposed to overcome these shortcomings (Reddy, 2000). Moreover, Nguyen *et al*. (2008) demonstrated that the TSDT is also capable of considering the stretching effect.

Meshless methods have gained increasing attention as powerful alternatives to traditional mesh-based techniques such as the finite element method (FEM) for analysis of plates (Konda *et al*. 2019, 2009). Unlike FEM, meshless approaches do not require predefined element connectivity, which makes them particularly effective for problems involving large deformations, discontinuities, evolving geometries, and functionally graded properties (Vakili *et al*. 2019). It is worth noting that the Element-Free Galerkin (EFG) method is among the most widely used meshless techniques. This method is formulated based on the global weak form of the governing differential equations. Although a background cell structure is employed for numerical integration, it does not require refinement when the nodal spacing is reduced to achieve higher accuracy in field approximation (Gu

et al. 2001). As a result, the EFG method exhibits a high convergence rate and generally requires less computational time compared to other meshless methods.

Shear locking is a numerical artifact commonly observed in finite element analysis of thin plate and shell structures, particularly when using low-order shear deformation theories (Khazri *et al*. 2018). It occurs when the assumed transverse shear strain field is overly constrained, leading to an artificially stiff response and an underestimation of deflections and stresses. In thin plates, the transverse shear strains should theoretically approach zero, however, standard finite element formulations often fail to reproduce this behavior, causing significant errors in both displacement and stress results. This phenomenon becomes more pronounced when modeling functionally graded plates, where material inhomogeneity introduces additional complexity in strain and stress distributions. Overcoming shear locking is therefore essential to accurately capture the bending response, especially when higher-order shear deformation theories are employed to account for realistic shear effects without resorting to shear correction factors.

In the present study, to enhance the Element-Free Galerkin (EFG) method and overcome limitations in modeling functionally graded plates based on higher-order shear deformation theory, a specific coupling relationship between the displacement and rotation fields is introduced. This relationship effectively links the rotational components to the transverse displacement field, serving as an efficient strategy to mitigate the excessive stiffness caused by shear locking 'a well-known issue in the Finite Element Method (FEM)' that has been adapted here for the EFG framework. Through this formulation, shear deformations are naturally constrained and tend to vanish in thin plates, thereby improving both the accuracy and numerical stability of the analysis.

Although numerous works have been published on the subject of thick FGPs, many existing methods either require a large number of unknowns, suffer from shear-locking, or do not efficiently integrate higher-order shear deformation theories with meshless methods. To address these limitations, the present study proposes a novel approach based on the EFG method combined with HSDT, which allows for accurate and efficient analysis of thick P-FGM plates while overcoming the issues mentioned above. Furthermore, a three-dimensional estimating function based on machine learning is employed to predict the central deflection, representing a new data-driven aspect of this work. This study therefore not only builds upon prior research but also provides methodological improvements and a clear extension of the existing literature, offering a comprehensive framework for the static response analysis of thick FGPs.

2. A mathematical simulation of the micromechanical properties of FGMs

Consider a FGP (as illustrated in Fig. 1(a)) with a length of a, a width of b and a thickness of h. The reference surface is defined as the mid-surface of the plate, with z=0 denoting the thickness coordinate measured from the undeformed mid-surface. It is assumed that the FGP is homogeneous and isotropic macroscopically. Furthermore, it is assumed that the upper surface ($z = +h/2$) of the plate is composed of a ceramic-rich material, while the lower surface ($z = -h/2$) is composed of a metal-rich material. This section, presents the fundamental equations of the power-law functionally graded material (P-FGM) in order to express the geometric configuration and to simulate the average or effective micromechanical properties of FGMs. The dual-phase material configuration comprises two isotropic components, ceramic and metal, which are randomly distributed on a microscopic scale. In this paper, it is assumed that the effective micromechanical properties of the FGPs vary continuously along the thickness, as illustrated in Fig. 1(b). In accordance with the rule of mixture

Table 2 Properties Test Report of the used steel 10 mm and 8mm bars (3 samples for each).

Mechanical Properties	Metal	Ceramics	
	Aluminum (Al)	Alumina (Al_2O_3)	Zirconia (ZrO_2)
Young modulus (E) (GPa)	70	380	151
Poisson's ratio (ν)	0.3	0.3	0.3

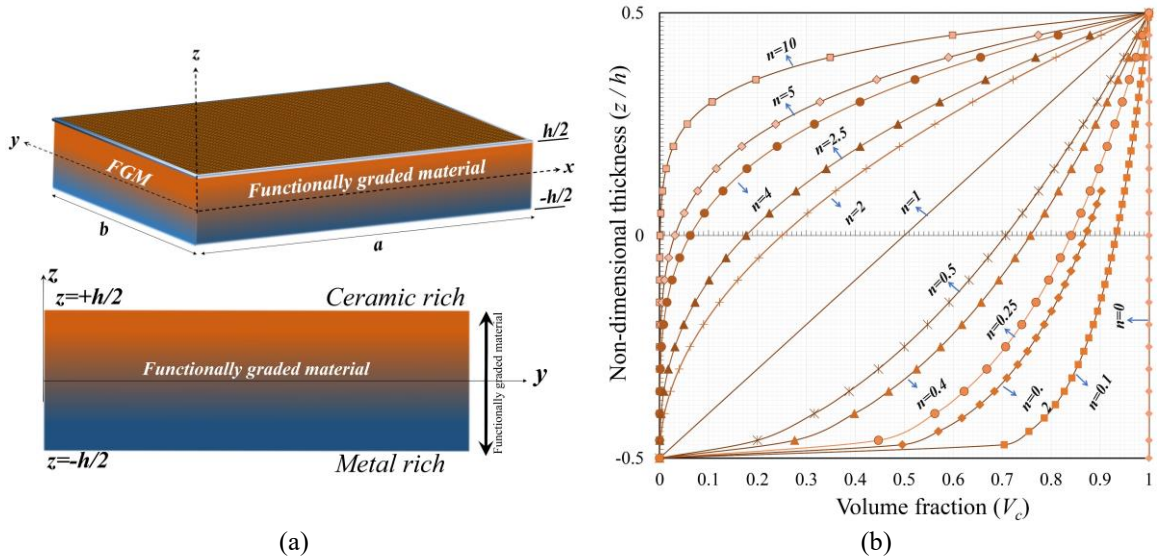

(a) (b)

Fig. 1 (a) Geometry and section of the P-FGP and (b) Variation of volume fraction of ceramic V_c with n index through the nondimensional thickness

based on power law distribution, the prediction of the average or effective micromechanical characteristics of FGP (P_{eff} variable) such as Young's modulus, Poisson's ratio and density along the thickness of the plate (z-axis direction) can be illustrated by the following equation (Reddy's power-Law) (Martínez-Pañeda 2019):

$$\begin{aligned} P_{eff}(z) &= P_m + V_c P_{CM} \\ V_c &= \left(\frac{z}{h} + \frac{1}{2}\right)^n \frac{-h}{2} \le z \le \frac{h}{2}, 0 \le n \le \infty \\ P_{CM} &= P_c - P_m V_m = 1 - V_c \end{aligned} \tag{1}$$

where P_c and P_m are the mechanical properties of the ceramic and metal respectively. Note that the subscripts m and c are used throughout the paper to denote ceramic and metal segments respectively. The power index n and the ceramic volume fraction, V_C are also considered. Eq. (2) indicates that the volume fraction varies in a manner that is dependent upon the power index n and thickness. If n is zero, the resulting structure is a ceramic-rich plate. Conversely, when n approaches infinity, the structure is a metal-rich plate. The region between the two surfaces consists of a mixture of both materials (as shown in Fig. 1(b)). In this paper, the mechanical properties for the metals and ceramics used in the P-FGP are listed in Table 1. It is presumed that the deformation process of the P-FGP structure occurs within the range of perfect elastic behavior.

3. Fundamental equations of thick P-FGPs

3.1 Review of Kinematics of the deformation field in HSDT

In this paper, the Reddy's HSDT (Reddy 2000) has been employed. As introduced by Nguyen *et al*. (2016), the HSDT posits that the approximation of the thickness stretching effect can be achieved by considering shear deformations. According to this theory, the displacement field of the P-FGP considering the effect of transverse normal stress is described as follows:

$$\begin{Bmatrix} u(x,y,z) \\ v(x,y,z) \\ w(x,y,z) \end{Bmatrix} = \begin{Bmatrix} u_0(x,y) + \phi_x(x,y)z - \xi_1 z^3 \underbrace{\left(\phi_x(x,y) + w_{0,x}(x,y)\right)}_{\Psi_x} \\ v_0(x,y) + \phi_y(x,y)z - \xi_1 z^3 \underbrace{\left(\phi_y(x,y) + w_{0,y}(x,y)\right)}_{\Psi_y} \left(-\frac{h}{2} \le z \le \frac{h}{2}\right) \\ w(x,y,z=0) = w_0(x,y), \xi_1 = \frac{4}{3h^2} \end{Bmatrix} \tag{2}$$

where $\{u, v, w\}$ denote the displacements of a point along the (*x*,*y*,*z*) coordinates, $\{u_0, v_0, w_0\}$ are corresponding displacements of a point on the mid-plane ($z = 0$), ϕ_x and ϕ_y are the rotations of a transverse normal about the *y*- and *x*-axes, respectively. The quantities Ψ_x and Ψ_y are the so-called warping functions. In this paper, it is assumed $\sigma_{zz} \approx 0$ (Reddy 2000).

3.2 Strains and stresses

The compact form of the strains field for HSDT is expressed as follows (Reddy 2000):

$$\begin{aligned} \{\hat{\varepsilon}\} &= \{\varepsilon_{xx}, \varepsilon_{yy}, \gamma_{xy}, \gamma_{xz}, \gamma_{yz}\}^T = \{\varepsilon^{(0)}\} + z\{\kappa^{(1)}\} + z^2\{\kappa^{(2)}\} + z^3\{\kappa^{(3)}\} \\ \{\hat{\varepsilon}\} &= \begin{cases} \varepsilon_{xx} = {\varepsilon^{(0)}}_{xx} + z\left(\kappa_{xx}^{(1)} + z^2\kappa_{xx}^{(3)}\right), \varepsilon_{yy} = {\varepsilon^{(0)}}_{yy} + z\left(\kappa_{yy}^{(1)} + z^2\kappa_{yy}^{(3)}\right) \\ \gamma_{xy} = {\varepsilon^{(0)}}_{xy} + z\left(\kappa_{xy}^{(1)} + z^2\kappa_{xy}^{(3)}\right), \gamma_{xz} = {\varepsilon^{(0)}}_{xz} + z^2\kappa_{xz}^{(2)} \\ \gamma_{yz} = {\varepsilon^{(0)}}_{yz} + z^2\kappa_{yz}^{(2)}, \varepsilon_{zz} = 0 \end{cases} \end{aligned} \tag{3}$$

where

$$\begin{cases} {\varepsilon^{(0)}}_{xx} = \dfrac{\partial u_0}{\partial x}, {\varepsilon^{(0)}}_{yy} = \dfrac{\partial v_0}{\partial y}, {\varepsilon^{(0)}}_{zz} = 0 \\ {\gamma^{(0)}}_{xy} = \dfrac{\partial u_0}{\partial y} + \dfrac{\partial v_0}{\partial x}, {\gamma^{(0)}}_{xz} = \dfrac{\partial \phi_x(x,y)}{\partial x} + \dfrac{\partial w_0(x,y)}{\partial x}, {\gamma^{(0)}}_{yz} = \dfrac{\partial \phi_y(x,y)}{\partial y} + \dfrac{\partial w_0(x,y)}{\partial y} \\ {\kappa^{(1)}}_{xx} = \dfrac{\partial \phi_x(x,y)}{\partial x}, {\kappa^{(1)}}_{yy} = \dfrac{\partial \phi_y(x,y)}{\partial y}, {\kappa^{(1)}}_{xy} = \dfrac{\partial \phi_x(x,y)}{\partial y} + \dfrac{\partial \phi_y(x,y)}{\partial x} \\ {\kappa^{(2)}}_{xz} = -\xi_2\left(\dfrac{\partial \phi_x(x,y)}{\partial x} + \dfrac{\partial w_0(x,y)}{\partial x}\right), {\kappa^{(2)}}_{yz} = -\xi_2\left(\dfrac{\partial \phi_y(x,y)}{\partial y} + \dfrac{\partial w_0(x,y)}{\partial y}\right), \xi_2 = \dfrac{4}{h^2} \\ {\kappa^{(3)}}_{xx} = -\xi_1\left(\dfrac{\partial \phi_x(x,y)}{\partial x} + \dfrac{\partial^2 w_0(x,y)}{\partial x^2}\right), {\kappa^{(3)}}_{yy} = -\xi_1\left(\dfrac{\partial \phi_y(x,y)}{\partial y} + \dfrac{\partial^2 w_0(x,y)}{\partial y^2}\right) \\ {\kappa^{(3)}}_{xy} = -\xi_1\left(\dfrac{\partial \phi_x(x,y)}{\partial y} + \dfrac{\partial \phi_y(x,y)}{\partial x} + 2\dfrac{\partial^2 w_0(x,y)}{\partial x \partial y}\right) \end{cases} \tag{4}$$

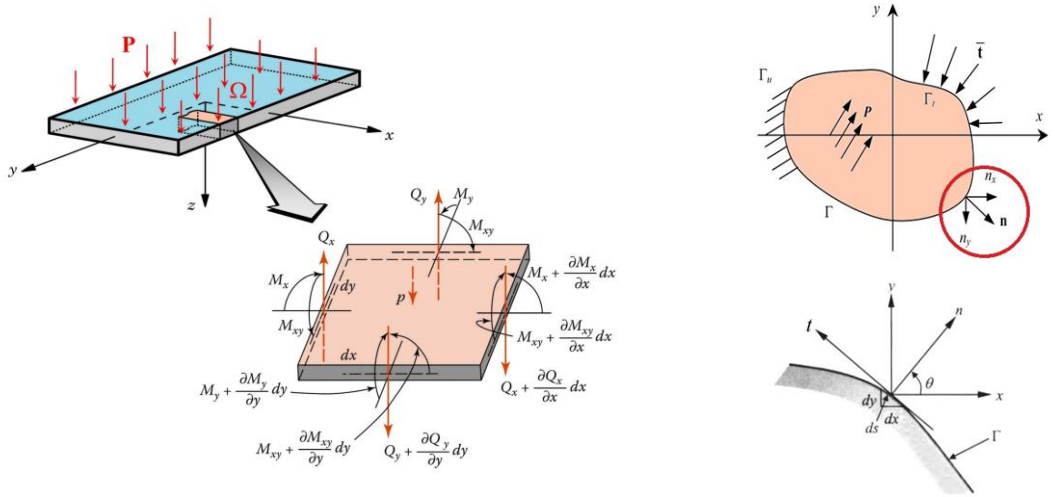

(a) (b)

Fig. 2 (a) Element of a thick P-FGP under the body force and (b) Essential boundary (Γ_u), Natural boundary (Γ_t) and boundary indicators

The compact inplane stresses field for HSDT is expressed as follows (Reddy 2000):

$$\{\hat{\sigma}\} = [\bar{Q}_{ij}(z)]\{\varepsilon^{(0)}\} + z[\bar{Q}_{ij}(z)]\{\kappa^{(1)}\} + z^2[\bar{Q}_{ij}(z)]\{\kappa^{(2)}\} + z^3[\bar{Q}_{ij}(z)]\{\kappa^{(3)}\} \tag{5}$$

where

$$[\bar{Q}(z)] = \begin{bmatrix} \frac{E_{eff}(z)}{1-\nu_{eff}(z)^2} & \frac{E_{eff}(z)\nu_{eff}(z)}{1-\nu_{eff}(z)^2} & 0 & 0 & 0 \\ \frac{E_{eff}(z)\nu_{eff}(z)}{1-\nu_{eff}(z)^2} & \frac{E_{eff}(z)}{1-\nu_{eff}(z)^2} & 0 & 0 & 0 \\ 0 & 0 & \frac{E_{eff}(z)}{2\left(1+\nu_{eff}(z)\right)} & 0 & 0 \\ 0 & 0 & 0 & \frac{E_{eff}(z)}{2\left(1+\nu_{eff}(z)\right)} & 0 \\ 0 & 0 & 0 & 0 & \frac{E_{eff}(z)}{2\left(1+\nu_{eff}(z)\right)} \end{bmatrix}_{\sigma_{zz}=0} \tag{6}$$

3.3 The Equilibrium equations of P-FGP

Consider the domain $\Omega \subset \mathbb{R}^2 \times \left(-\frac{h}{2}, \frac{h}{2}\right)$ of thick P-FGP that include of nodes scattered and bounded by $\Gamma = \Gamma_t \cup \Gamma_u$ where Γ_t denotes the traction boundaries and Γ_u denotes the essential boundary. The equilibrium equations that govern the element of FGP, as illustrated in Fig. 2, are as follows (Reddy 2000):

$$\sum F_X = 0 \Rightarrow \frac{\partial Q_x}{\partial x} + \frac{\partial Q_y}{\partial y} = -P \tag{7}$$

$$\sum M_X = 0 \Rightarrow \frac{\partial M_y}{\partial y} + \frac{\partial M_{xy}}{\partial x} = Q_y \tag{8}$$

$$\sum M_y = 0 \Rightarrow \frac{\partial M_x}{\partial x} + \frac{\partial M_{yx}}{\partial y} = Q_x \tag{9}$$

4. EFG formulation of the static flexure problem of FGP

4.1 Weak form equations

The Galerkin weak formulation of thick FGPs is as follows (Liu 2009):

$$\iint_\Omega (\delta(L_d u)^T \bar{Q} L_d u) d\Omega = \iint_\Omega P\hat{w} d\Omega + \int_S Q_n \hat{w} dS + \int_S \left(M_n \hat{\phi}_n\right) dS + \int_S \left(M_t \hat{\phi}_t\right) dS \tag{10}$$

where $\{\hat{w}, \hat{\phi}_x, \hat{\phi}_y\}$ represent the weight function of transverse displacement and rotation, respectively and the nodal deformation field is defined as follows:

$$u^T = \{w \quad \phi_x \quad \phi_y\} \tag{11}$$

Also, L_d is defined as follows:

$$L_d = \begin{bmatrix} -\xi_1 z^3 \dfrac{\partial^2}{\partial x^2} & (z - \xi_1 z^3)\dfrac{\partial}{\partial x} & 0 \\ -\xi_1 z^3 \dfrac{\partial^2}{\partial y^2} & 0 & (z - \xi_1 z^3)\dfrac{\partial}{\partial y} \\ -2\xi_1 z^3 \dfrac{\partial^2}{\partial x \partial y} & (z - \xi_1 z^3)\dfrac{\partial}{\partial y} & (z - \xi_1 z^3)\dfrac{\partial}{\partial x} \\ (1 - \xi_2 z^2)\dfrac{\partial}{\partial x} & (1 - \xi_2 z^2) & 0 \\ (1 - \xi_2 z^2)\dfrac{\partial}{\partial y} & 0 & (1 - \xi_2 z^2) \end{bmatrix} \tag{12}$$

4.2 The RPIM shape functions

The field variables are defined as deviations and rotations in all nodes as follows (Liu, 2009):

$$\begin{aligned} w(x,y) &= \sum_{i=1}^{np} \varphi_i w_i, \phi_x(x,y) = \sum_{i=1}^{np} \varphi_{xi} \phi_{xi}, \phi_y(x,y) \\ &= \sum_{i=1}^{np} \varphi_{yi} \phi_{yi}, \varphi_{xi}(x,y) = \frac{\partial \varphi_i(x,y)}{\partial x}, \varphi_{yi}(x,y) = \frac{\partial \varphi_i(x,y)}{\partial y} \end{aligned} \tag{13}$$

where φ_i, φ_{xi}, and φ_{yi} are the shape functions for the three field variables$w$, ϕ_{xi}, and ϕ_{yi}. As introduced by Liu (2009), φ_{xi} and φ_{yi} are independent of each other and do not have to be the

same. Also, in this paper, the shape functions of rotations are constructed based on the first derivatives of the shape functions of transverse displacement. This approach helps to effectively avoid the shear-locking phenomenon. Equation (13) can be expressed in the following matrix form (Vakili *et al*. 2021, Liu, 2009):

$$u = \begin{Bmatrix} w \\ \phi_x \\ \phi_y \end{Bmatrix} = \sum_{i=1}^{n} \underbrace{\begin{bmatrix} \varphi_i & 0 & 0 \\ 0 & \varphi_{xi} & 0 \\ 0 & 0 & \varphi_{yi} \end{bmatrix}}_{\Phi_i} \underbrace{\begin{Bmatrix} w_i \\ \phi_{xi} \\ \phi_{yi} \end{Bmatrix}}_{U_i} = \Phi_i U_i \tag{14}$$

where Matrix Φ_i contains the shape functions arranged and U_i is the vector of nodal variables for node ***i***-th. In this study, the RPIM approximation is used to approximate all these field variables w_0, ϕ_{xi} and ϕ_{yi}. According to the Eq. (3), the matrix form of the strain-displacement relationship is as follows (Vakili *et al*. 2021, Liu 2009):

$$U^h(x, x_Q) = \sum_{i=1}^{np} R_i(x,y) a_i(x_Q) = R^T a(x_Q) \tag{15}$$

where

$$\{a(x_Q)\}^T = \{a_1 \quad a_2 \quad \dots \quad a_n\} \quad R^T = [R_1(x,y), R_2(x,y), \dots, R_n(x,y)] \tag{16}$$

$$R_i(x,y) = (r_i^2 + C^2) \rightleftarrows^q \qquad r_i = \sqrt{(x-x_i)^2 + (y-y_i)^2} \qquad C = \alpha_c . d_c$$
$$where \quad q \cong 1.99 \quad \alpha_c = 6 \tag{17}$$

where r_i is the distance between the sampling point x_i.

$$\bar{U} = \{ U_1 \quad U_2 \quad \dots \quad U_i|_{i=1}^{np} \}^T = \{ w_{01} \ \phi_{x1} \ \phi_{y1} \quad w_{02} \ \phi_{x2} \ \phi_{y2} \quad \dots\dots \quad w_{0i} \ \phi_{xi} \ \phi_{yi}|_{i=1}^{np} \}^T \tag{18}$$

$$\bar{U} = R_Q a \rightarrow a = R_Q^{-1} \bar{U} \tag{19}$$

where R_Q is the moment matrix:

$$R_Q = \begin{bmatrix} R_1(r_1) & R_2(r_1) & \cdots & R_{np}(r_1) \\ R_1(r_2) & R_2(r_2) & \cdots & R_{np}(r_2) \\ \vdots & \vdots & \ddots & \vdots \\ R_1(r_{np}) & R_2(r_{np}) & \cdots & R_{np}(r_{np}) \end{bmatrix}_{(np \times np)} \tag{20}$$

Therefore, can be written as (Vakili *et al*. 2021, Liu 2009):

$$\begin{aligned} U^h(x,y) &= \underbrace{R^T(x,y) R_Q^{-1}}_{\widehat{\Phi}(x,y)} \bar{U} = \widehat{\Phi}(x,y) \bar{U} \\ &= \{ \widehat{\Phi}_1(x,y) \quad \widehat{\Phi}_2(x,y) \quad \widehat{\Phi}_3(x,y) \dots\dots \quad \widehat{\Phi}_{np}(x,y) \} \bar{U} \end{aligned} \tag{21}$$

In which $\widehat{\Phi}_i(x,y)$is the shape function for the i-th node. Finally, the RPIM shape functions corresponding to the transverse displacement and rotations of the i-th node can be obtained as follows (Vakili *et al*. 2021, Liu 2009):

$$\widehat{\Phi}_i(x,y) = \begin{bmatrix} \widehat{\Phi}_i(x,y) & 0 & 0 \\ 0 & \widehat{\Phi}_{i,x}(x,y) & 0 \\ 0 & 0 & \widehat{\Phi}_{i,y}(x,y) \end{bmatrix} \tag{22}$$

Substituting the Eq. (22) into Eq. (21), one can write:

$$U^h(x) = \widehat{\Phi}(x,y)\bar{U} = \sum_{i=1}^{np} \widehat{\Phi}_i(x,y)U_i = \sum_{i=1}^{np} \begin{bmatrix} \widehat{\Phi}_i(x,y) & 0 & 0 \\ 0 & \widehat{\Phi}_{i,x}(x,y) & 0 \\ 0 & 0 & \widehat{\Phi}_{i,y}(x,y) \end{bmatrix} \begin{Bmatrix} w_{0i} \\ \phi_{xi} \\ \phi_{yi} \end{Bmatrix} \tag{23}$$

The first and the second derivative of shape functions with RPIM can be written as follows (Vakili *et al*. 2021, Liu 2009):

$$\begin{aligned}
\widehat{\Phi}_{i,x} &= \frac{\partial \widehat{\Phi}}{\partial x} = \sum_{i=1}^{np} \frac{\partial R_i}{\partial x} = \sum_{i=1}^{np} [2q(r_i^2 + C^2)^{q-1}(x - x_i)] \\
\widehat{\Phi}_{i,y} &= \frac{\partial \widehat{\Phi}}{\partial y} = \sum_{i=1}^{np} \frac{\partial R_i}{\partial y} = \sum_{i=1}^{np} [2q(r_i^2 + C^2)^{q-1}(y - y_i)] \\
\widehat{\Phi}_{i,xx} &= \frac{\partial^2 \widehat{\Phi}}{\partial x^2} = \sum_{i=1}^{np} \frac{\partial^2 R_i}{\partial x^2} = \sum_{i=1}^{np} [2q(r_i^2 + C^2)^{q-1} + 4q(q-1)(r_i^2 + C^2)^{q-2}(x - x_i)^2] \\
\widehat{\Phi}_{i,yy} &= \frac{\partial^2 \widehat{\Phi}}{\partial y^2} = \sum_{i=1}^{np} \frac{\partial^2 R_i}{\partial y^2} = \sum_{i=1}^{np} [2q(r_i^2 + C^2)^{q-1} + 4q(q-1)(r_i^2 + C^2)^{q-2}(y - y_i)^2] \\
\widehat{\Phi}_{i,xy} &= \frac{\partial^2 \widehat{\Phi}}{\partial xy} = \sum_{i=1}^{np} \frac{\partial^2 R_i}{\partial x \partial y} = \sum_{i=1}^{np} [4q(q-1)(r_i^2 + C^2)^{q-2}(x - x_i)(y - y_i)]
\end{aligned} \tag{24}$$

The Galerkin-weak form of the bending equation of plates with Lagrange multipliers for the constraints is given by the following equation (Vakili *et al*. 2021, Liu 2009):

$$\begin{aligned}
&\int_\Omega \delta((L_d U^h)^T \bar{Q}(z)(L_d U^h) d\Omega - \int_\Omega (\delta U^h)^T P d\Omega - \ldots. \\
&\ldots - \int_{\Gamma_t} (\delta U^h)^T d\Gamma_t - \int_{\Gamma u} \delta\vartheta^T (U^h - u_\Gamma) d\Gamma - \int_{\Gamma u} \delta {U^h}^T \vartheta d\Gamma = 0
\end{aligned} \tag{25}$$

where the term u_Γ denotes the prescribed displacement on the essential boundaries Γ_u, the ϑ is Lagrange multipliers also the displacement vector U^h has been obtained by the Eq. (23). The $L_d U^h$ term for HSDT given as follows:

$$L_d U^h = \left[\sum_{i=1}^{np} \begin{bmatrix} -\xi_1 z^3 \frac{\partial^2}{\partial x^2} & (z - \xi_1 z^3)\frac{\partial}{\partial x} & 0 \\ -\xi_1 z^3 \frac{\partial^2}{\partial y^2} & 0 & (z - \xi_1 z^3)\frac{\partial}{\partial y} \\ -\xi_1 z^3 \frac{\partial^2}{\partial x \partial y} & (z - \xi_1 z^3)\frac{\partial}{\partial y} & (z - \xi_1 \rightleftarrows z^3)\frac{\partial}{\partial x} \\ (1 - \xi_2 . z^2)\frac{\partial}{\partial x} & (1 - \xi_2 z^2) & 0 \\ (1 - \xi_2 . z^2)\frac{\partial}{\partial y} & 0 & (1 - \xi_2 z^2) \end{bmatrix} \times \ldots \right.$$
$$\left. \underbrace{\ldots \times \begin{bmatrix} \widehat{\Phi}_i(x,y) & 0 & 0 \\ 0 & \widehat{\Phi}_{i,x}(x,y) & 0 \\ 0 & 0 & \widehat{\Phi}_{i,y}(x,y) \end{bmatrix}}_{\sum_{i=1}^{np}(B)_i} \right] \times \begin{Bmatrix} w_{0i} \\ \phi_{xi} \\ \phi_{yi} \end{Bmatrix} = \sum_{i=1}^{np} (B)_i U_i \tag{26}$$

where

$$\vartheta(\hat{x}) = \sum_{i \in S_\vartheta} \widetilde{N}_i(s)\vartheta_i \qquad \hat{x} \in \Gamma_u \tag{27}$$

$$\widetilde{N}_k^r(s) = \prod_{\substack{i=0 \\ i \neq k}}^{r} \frac{(s - s_i)}{(s_k - s_i)} \tag{28}$$

Therefore can write:

$$\vartheta = \sum_{i \in S_\vartheta} \underbrace{\begin{bmatrix} \widetilde{N}_i & 0 & 0 \\ 0 & \widetilde{N}_i & 0 \\ 0 & 0 & \widetilde{N}_i \end{bmatrix}}_{\bar{N}_i} \underbrace{\begin{Bmatrix} \vartheta_{w_{0i}} \\ \vartheta_{\psi_{xi}} \\ \vartheta_{\psi_{yi}} \end{Bmatrix}}_{\vartheta_i} = \sum_{i \in S_\vartheta} \bar{N}_i \vartheta_i \tag{29}$$

Substituting Eq. (26) into Eq. (25), one can write:

$$\begin{aligned} &\int_\Omega \delta \left(\sum_{i=1}^{n \in S_n} B_i u_i \right)^T \bar{Q}(z) \left(\sum_{j=1}^{n \in S_n} B_j u_j \right) d\Omega - \int_\Omega \delta \left(\sum_{i=1}^{n \in S_n} \hat{\Phi}_i u_i \right)^T P d\Omega - \int_{\Gamma_t} \delta \left(\sum_{i=1}^{n \in S_n} \hat{\Phi}_i u_i \right)^T \bar{t} d\Gamma - \ldots . \\ &\int_{\Gamma_u} \delta\vartheta^T \left(\left(\sum_{i=1}^{n \in S_n} \Phi_i (U_h)_i \right) - u_\Gamma \right) d\Gamma - \int_{\Gamma_u} \delta \left(\sum_{i=1}^{n \in S_n} \Phi_i (U_h)_i \right)^T \vartheta d\Gamma = 0 \end{aligned} \tag{30}$$

$$\begin{aligned} &\int_{\boldsymbol{\Omega}} \boldsymbol{\delta} \left(\sum_{i \in S_n} \boldsymbol{B}_i u_i \right)^T \overline{Q}(z) \left(\sum_{j \in S_n} \boldsymbol{B}_j u_j \right) d\boldsymbol{\Omega} = \int_{\boldsymbol{\Omega}} \boldsymbol{\delta} \left(\sum_{i \in S_n} u_i^T \boldsymbol{B}_i^T \right) \overline{Q}(z) \left(\sum_{j \in S_n} \boldsymbol{B}_j u_j \right) d\boldsymbol{\Omega} \rightarrow \ldots \\ &\int_{\boldsymbol{\Omega}} \boldsymbol{\delta} \left(\sum_{i \in S_n} u_i^T \boldsymbol{B}_i^T \right) \overline{Q}(z) \left(\sum_{j \in S_n} \boldsymbol{B}_j u_j \right) d\boldsymbol{\Omega} = \sum_{i \in S_n} \sum_{j \in S_n} \boldsymbol{\delta} u_i^T \underbrace{\int_{\boldsymbol{\Omega}} \boldsymbol{B}_i^T \overline{Q}(z) \boldsymbol{B}_j d\boldsymbol{\Omega}}_{\boldsymbol{K}_{ij}} u_j = \ldots \\ &\ldots = \sum_{i \in S_n} \sum_{j \in S_n} \boldsymbol{\delta} u_i^T \boldsymbol{K}_{ij} u_j, \quad \text{where} \quad \boldsymbol{K}_{ij} = \int_{\boldsymbol{\Omega}} \boldsymbol{B}_i^T \overline{Q}(z) \boldsymbol{B}_j d\boldsymbol{\Omega} \end{aligned} \tag{31}$$

where K_{ij} is nodal stiffness matrix.

$$\int_\Omega \delta \left(\sum_{i=1}^{n \in S_n} \hat{\Phi}_i u_i \right)^T P d\Omega = \sum_{i \in S_n} \delta u_i^T \int_\Omega \left(\hat{\Phi}_i \right)^T P d\Omega = \sum_{i \in S_n} \delta u_i^T f_i = \delta \bar{U}^T \bar{F}_\Omega \tag{32}$$

$$\begin{aligned} &\int_{\Gamma_u} \delta \left(\sum_{i \in S_n} \hat{\Phi}_i u_i \right)^T \vartheta d\Gamma = \int_{\Gamma_u} \delta \left(\sum_{i \in S_n} \hat{\Phi}_i u_i \right)^T \left(\sum_{j \in S_n} \bar{N}_j \vartheta_j \right) d\Gamma = \sum_{i \in S_n} \sum_{j \in S_\lambda} \delta u_i^T \underbrace{\int_{\Gamma_u} \left(\hat{\Phi}_i \right)^T \bar{N}_j d\Gamma}_{-G_{ij}} \vartheta_j \\ &= \ldots\ldots - \sum_{i \in S_n}^{n} \sum_{j \in S_n}^{n\vartheta_t} \delta u_i^T G_{ij} \vartheta_j = -\delta \bar{U}^T G \vartheta \end{aligned} \tag{33}$$

$$G_{ij} = -\int_{\Gamma_u} \left(\widehat{\Phi}_i\right)^T N_j d\Gamma \tag{34}$$

Finally, it can be written:

$$\underbrace{\int_{\Omega} \delta \left(\sum_{i\in S_n} (B)_i u_i\right)^T \bar{Q}(z) \left(\sum_{j\in S_n} (B)_j u_j\right) d\Omega}_{\delta U^T K U} - \underbrace{\int_{\Omega} \delta \left(\sum_{i\in S_n} \widehat{\Phi}_i u_i\right)^T P d\Omega - \int_{\Gamma_t} \delta \left(\sum_{i\in \delta_n} \widehat{\Phi}_i u_i\right)^T t^e d\Gamma}_{\delta U^T F} \dots$$
$$\underbrace{- \int_{\Gamma_u} \delta\vartheta^T \left(\left(\sum_{i\in S_n} \widehat{\Phi}_i u_i\right) - u_\Gamma\right) d\Gamma}_{\delta\vartheta^T [G^T \bar{U} - q]} \underbrace{- \int_{\Gamma_u} \delta \left(\sum_{i\in S_n} \widehat{\Phi}_i u_i\right)^T \vartheta d\Gamma = 0}_{\delta \bar{U}^T G \vartheta} \tag{35}$$

The vector q_i can be defined as follows (Vakili *et al*. 2021, Liu 2009):

$$q_i = -\int_{\Gamma_u} \bar{N}_i^T u_\Gamma d\Gamma \tag{36}$$

which is:

$$\delta U^T [K\bar{U} + G\vartheta - F] + \delta\vartheta^T [G^T \bar{U} - q] = 0 \tag{37}$$

Considering the arbitrary nature of $\partial U$and $\partial\vartheta$, it follows that the equation can only be satisfied if:

$$\begin{bmatrix} K & G \\ G^T & 0 \end{bmatrix} \begin{Bmatrix} \bar{U} \\ \vartheta \end{Bmatrix} = \begin{Bmatrix} F \\ q \end{Bmatrix} \tag{38}$$

Note: To calculate the integral in Eq. (37) and Eq. (38), it is necessary to discretize the problem domain into a set of background cells. Consequently, a global integration can be expressed as a summation of integrals over the aforementioned cells (Vakili *et al*. 2021):

$$\int_{\Omega} \Re d\Omega = \sum_{K}^{n_c} \int_{\Omega_K} \Re d\Omega \tag{39}$$

where n_c represents the number of background cells, $\Re$denotes the integrand, and $\Omega_K$signifies the domain of the ***k***-th background cell. The Gauss quadrature scheme, which is commonly employed in the FEM, is utilized to perform the integrations numerically over these cells. When n_gGauss points are employed within each background cell, the resulting equation is given by Eq. (39).

$$\int_{\Omega} \Re d\Omega = \sum_{K}^{n_c} \int_{\Omega_K} \Re d\Omega = \sum_{K}^{n_c} \sum_{i=1}^{n_g} \widehat{W}_i \Re(x_{Qi}) |J_{iK}^D| \tag{40}$$

where $\widehat{W}_i$ represents the Gauss weighting factor for the i-th Gauss point at x_{Qi} and J_{iK}^D is the Jacobian matrix for the area integration of the background cell `***k***`, in which the Gauss point x_{Qi} is located. The essential boundary conditions for simply supported edges 'Γ_{SS}' is given as follow (Vakili *et al*. 2021):

$$w|at \quad edges = 0, \phi_t|at \quad edges = 0 \tag{41}$$

The essential boundary conditions for clamped supported edges 'Γ_{CS}' is given as follow (Vakili *et al*. 2021):

$$w|at \quad edges = 0, \phi_n|at \quad edges = 0, \phi_t|at \quad edges = 0, \frac{\partial w}{\partial n}|at \quad edges = 0 \tag{42}$$

where ϕ_n is the rotation with respect to the axis parallel to the normal direction of the boundary. RPIM matrix $\left(\bar{\Phi}_{i_i}\right)$ for the simply and clamped supported edges as follow (Vakili *et al*. 2021):

For simply support:

$$\bar{\Phi}_i = \begin{bmatrix} \hat{\Phi}_i & 0 & 0 \\ 0 & 0 & 0 \\ 0 & 0 & 0 \end{bmatrix} \tag{43}$$

For clamped support:

$$\bar{\Phi}_{i_i} = \begin{bmatrix} \hat{\Phi}_i & 0 & 0 \\ 0 & \hat{\Phi}_{i,t} & 0 \\ 0 & 0 & \hat{\Phi}_{i,n} \end{bmatrix} \tag{44}$$

$$\hat{\Phi}_{i,n} = n_x \hat{\Phi}_{i,x} + n_y \hat{\Phi}_{i,y} \qquad \hat{\Phi}_{i,t} = n_x \hat{\Phi}_{i,y} - n_y \hat{\Phi}_{i,x} \tag{45}$$

The flowchart of EFG method for analysis of thick FGPs is shown in Fig. 3.

By solving the system of Eq. (38), the nodal displacements vector '$\bar{U}$' can be derived. Then, by substituting the nodal displacements into Eq. (14), the transverse displacement and the rotation functions 'u', 'φ_x', and 'φ_y' are obtained. Once the transverse displacement and the rotation functions have been determined, the strain vector can be calculated using the strain-displacement relationship 'Eq. (4)'. By substituting the obtained strains into the stress-strain relationship (Eq. 5), the stress vector is computed. The position of the neutral axis corresponds to the location where the first component of the stress vector, i.e. σ_{xx}, becomes zero.

5. Numerical results and discussions

The following section demonstrates the efficacy of the EFG method for the bending analysis of a range of thick P-FGP. The numerical examples presented subsequently consider two distinct types of FGPs, namely those comprising Al/ZrO_2 and Al/Al_2O_3. The Young modulus and Poisson's ratio for aluminum, zirconia and alumina have been defined in Table 1 for the purposes of this study.

First, presents the capability, accuracy, and convergence of the Element-Free Galerkin (EFG) method for analyzing the bending behavior of thick P-FGP (Al/ZrO_2) with supported boundary conditions (SSSS). then, the effect of nodal distribution on the results of the thick P-FGP (Al/ZrO_2) analysis using the EFG method with a varying number of nodes (25 to 441), the Enhanced Moving Kriging Interpolation (EMKI)-based Meshfree Method with a varying number of nodes (25 to 441), and the FEM using four-node elements was investigated. Nonlinear transverse loading in the form of $q(x,y) = q_0 Cos\,\pi/a\,(x - a/2) Sin(-\pi y/b)$ is applied to the thick FGP. To determine the effective mechanical properties of the FGP, Reddy's Power Law Homogenizer Function $P_{eff}(z)$ was used in Eq. (1). The analysis results, along with the error terms (values in parentheses), for the thick P-FGP (Al/ZrO_2) under the conditions $a/h = 10, b/a = 1$and $\boldsymbol{n}$=2 is provided in Table 2.

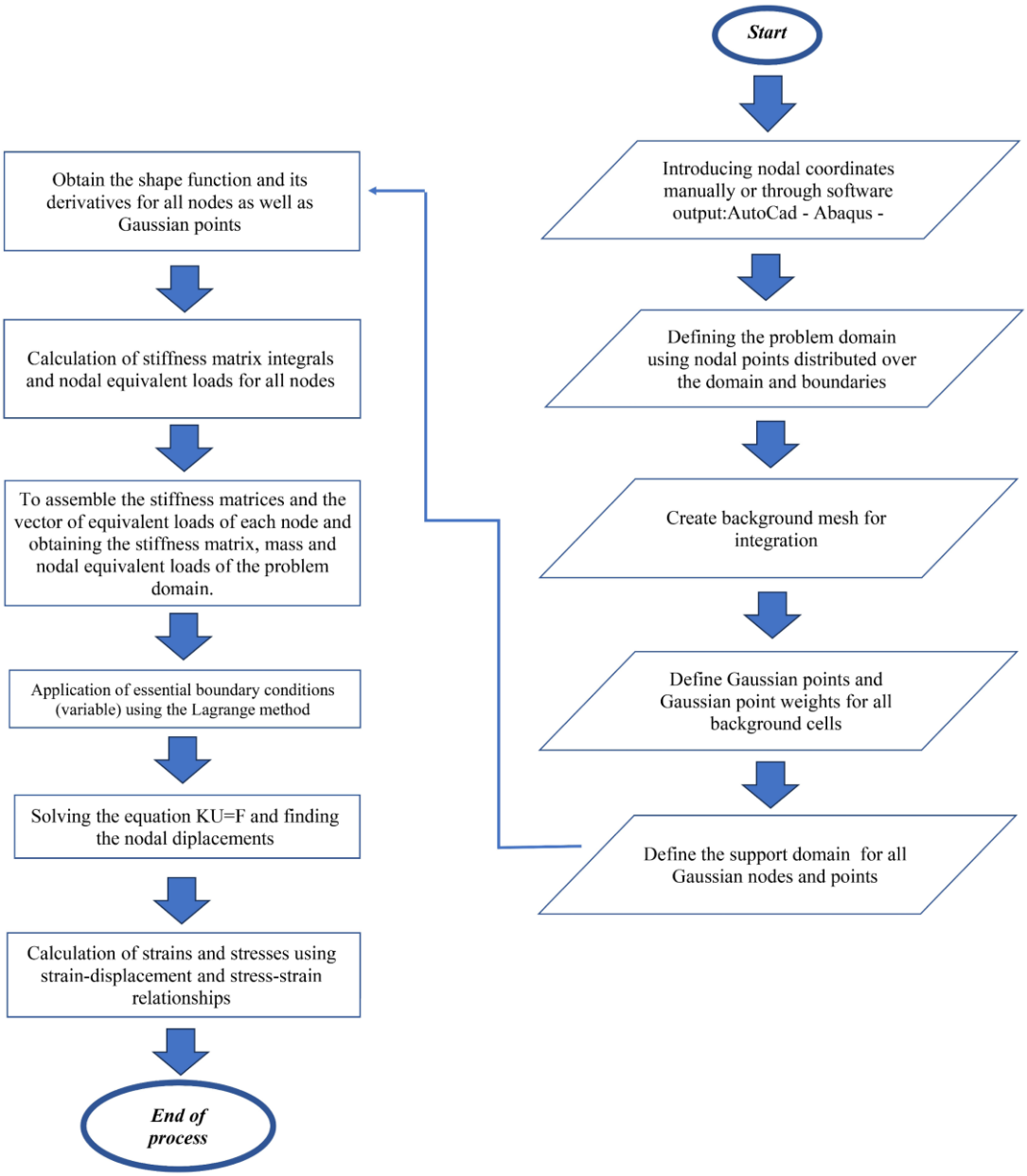

Fig. 3 The flowchart of EFG method for analysis of thick FGPs

The geometric properties and the variation of the ceramic volume fraction along the thickness based on the power-law index are illustrated in Fig. 1. To calculate the percentage error of the EFG, EMKI, and FEM methods, Eq. (46):

$$\text{Error } (\%) = \left| \frac{\left(W^{*\text{Ref}} - W^{*\text{Method}}\right)}{W^{*\text{Ref}}} \right| \times 100 \tag{46}$$

Table 2 Values of W^* for the FGP(Al/ZrO_2) under the condition (a/h = 10, n =2.0)

FEM		EMKI, q=1.03, a_c=2.5				Present, q=1.99, a_c=6			
4-node Elements (Dai *et al.* [redacted])	$W^*\times10^{-2}$ (Dai *et al.* 2004) Error%	Regular nodes	$W^*\times10^{-2}$ (Dai *et al.* 2004) Error %	Irregular nodes	$W^*\times10^{-2}$	Regular nodes	$W^*\times10^{-2}$ Error %	Irregular nodes	$W^*\times10^{-2}$ Error %
4×4	2.440 (47.15)	5×5	4.266 (7.63)	25	4.264 (7.66)	5×5	4.451 (3.6)	25	4.452 (3.6)
6×6	3.305 (28.42)	7×7	4.382 (5.11)	49	4.415 (4.40)	7×7	4.461 (3.4)	49	4.453 (3.56)
8×8	3.775 (18.25)	9×9	4.496 (2.65)	81	4.527 (1.97)	9×9	4.465 (3.31)	81	4.458 (3.45)
10×10	4.041 (12.50)	11×11	4.538 (1.72)	121	4.566 (1.12)	11×11	4.601 (0.36)	121	4.595 (0.49)
12×12	4.201 (9.02)	13×13	4.563 (1.18)	169	4.586 (0.69)	13×13	4.615 (0.06)	169	4.603 (0.31)
14×14	4.305 (6.78)	15×15	4.578 (0.86)	225	4.598 (0.44)	15×15	4.617 (0.02)	225	4.615 (0.07)
16×16	4.374 (5.27)	17×17	4.588 (0.65)	289	4.605 (0.27)	17×17	4.618 (0.00)	289	4.615 (0.62)
20×20	4.459 (3.43)	21×21	4.599 (0.40)	441	4.614 (0.08)	21×21	4.618 (0.00)	441	4.617 (0.02)

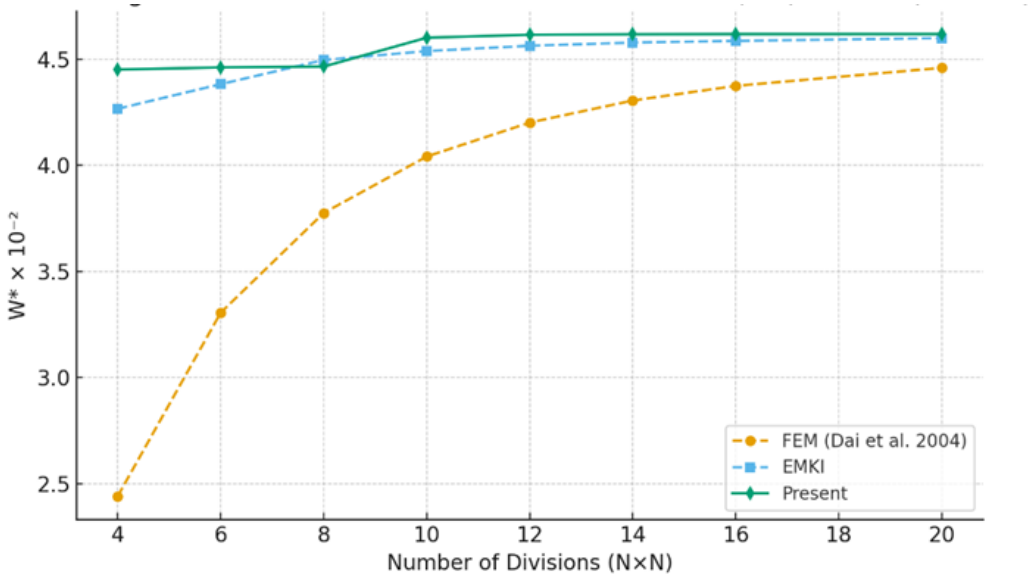

Fig. 4 Convergence of the proposed method for dimensionless central deflection

Table 3 Comparison between the results of W^* and $\sigma^*{}_{xx}$ for the P-FGP(Al/Al_2O_3) obtained from FSDT (with shear locking) and TSDT (without shear locking) under sinusoidal loading. (*a/h*=100 and *b/a*=1)

n	Method	W^*	$\sigma^*{}_{xx}(h/3)$
1	Present 11^2 node FSDT (With shear locking)	0.5357	14.108
	Present 11^2 node HSDT (Without shear locking)	0.5631	14.967
	Quasi-3D (Neves *et al*. 2012a)	0.5624	14.969
	Quasi-3D (Neves *et al*. 2012b)	0.5648	14.944
	Quasi-3D (Neves *et al*. 2013)	0.5647	14.945
	HSDT (Thai *et al*. 2013)	0.5625	14.969
	Quasi-3D (Carrera *et al*. 2011)	0.5625	14.969
	HSDT (Belabed *et al*. 2014)	0.5461	14.6762
4	Present 11^2 node FSDT (With shear locking)	0.7126	11.091
	Present 11^2 node	0.8184	11.702
	Quasi-3D (Neves *et al*. 2012a)	0.8286	11.932
	Quasi-3D (Neves *et al*. 2012b)	0.8241	11.738
	Quasi-3D (Neves *et al*. 2013)	0.824	11.737
	HSDT (Thai *et al*. 2013)	0.8286	11.923
	Quasi-3D (Carrera *et al*. 2011)	0.8286	11.923
	HSDT (Belabed *et al*. 2014)	0.7934	11.5443
10	Present 11^2 node FSDT (With shear locking)	0.8148	8.0261
	Present 11^2 node	0.9261	8.668
	Quasi-3D (Neves *et al*. 2012a)	0.8286	8.602
	Quasi-3D (Neves *et al*. 2012b)	0.9228	8.6013
	Quasi-3D (Neves *et al*. 2013)	0.9227	8.601
	HSDT (Thai *et al*. 2013)	0.9361	8.6077
	Quasi-3D (Carrera *et al*. 2011)	0.9361	8.6077
	HSDT (Belabed *et al*. 2014)	0.9135	8.7215

where $W^{*Ref} = 0.046183$ represents the analytical dimensionless transverse displacement provided in reference (Zenkour, 2006) and $W^{*Method}$ represents the dimensionless transverse displacement obtained from the EFG, EMKI, and FEM methods. The dimensionless transverse displacement and stresses are defined by Eq. (47):

$$W* = \frac{10E_c h^3}{q_0 a^4} W\left({}^{a}/_{2}, {}^{b}/_{2}, 0\right), \sigma^*{}_{xx}(z) = \frac{h}{q_0 a}\sigma_{xx}\left({}^{a}/_{2}, {}^{b}/_{2}, z\right)$$
$$\sigma^*{}_{xy}(z) = \frac{h}{q_0 a}\sigma_{xy}(0,0,z), \sigma^*{}_{xz}(z) = \frac{h}{q_0 a}\sigma_{xz}\left(0, {}^{b}/_{2}, z\right) \quad (47)$$

The analysis results are presented in Table 2. The comparison of results shows that the nodal arrangement's influence on the accuracy and convergence rate of the EFG method is minimal. Both regular and irregular nodal distributions achieve acceptable convergence with significantly fewer

Table 4 Values of W^*, σ^*_{xx}, $\sigma^*_{xy}$and σ^*_{xz} for the P-FGP(Al/Al_2O_3) under sinusoidal loading and *a*/*h*=10 and *b*/*a*=1

n	Method	*u*	W^*	$\sigma^*_{xx}(h/3)$	$\sigma^*_{xy}(-h/3)$	$\sigma^*_{xz}(h/6)$
1	Present 11^2 node	0.6415	0.5892	1.4896	0.6108	0.2581
	SSDT (Zenkour 2006)	0.6626	0.5889	1.4894	0.611	0.2622
	HSDT (Nguyen 2015)	0.6401	0.5883	1.4892	0.611	0.2552
	ITSDT (*Kulkarni et al*. 2015)	0.6402	0.5884	1.4891	0.611	0.2582
	TSDT (Wu *et al*. 2010)	0.6414	0.589	1.4898	0.6111	0.2599
	HSDT (Mantari *et al*. 2012)	0.6398	0.588	1.4888	0.6109	0.2566
	HSDT (Thai *et al*. 2013)	0.6414	0.589	1.4898	0.6111	0.2608
	Quasi-3D (Carrera *et al*. 2008)	0.6436	0.5875	1.5062	0.6081	0.251
	Quasi-3D (Wu *et al*. 2011)	0.6436	0.5876	1.5061	0.6112	0.2511
	Quasi-3D (Neves *et al*. 2012a)	-	0.5845	1.4945	-	-
	Quasi-3D (Neves *et al*. 2012b)	-	0.5868	1.4917	-	-
	Quasi-3D (Neves *et al*. 2013)	-	0.5868	1.4917	-	-
	Quasi-3D (Carrera *et al*. 2011)	-	0.5875	1.5064	-	-
	HSDT (Belabed *et al*. 2014)	-	0.5895	1.4677	-	-
2	Present 11^2 node	0.8985	0.7573	1.3981	0.5445	0.2723
	SSDT (Zenkour 2006)	0.9281	0.7573	1.3954	0.5441	0.2763
	HSDT (Nguyen 2015)	0.8961	0.7567	1.3947	0.5439	0.2721
	ITSDT (Kulkarni *et al*. 2015)	0.8963	0.7569	1.3946	0.5439	0.2748
	TSDT (Wu *et al*. 2010)	0.8984	0.7573	1.396	0.5442	0.2721
	HSDT (Mantari *et al*. 2012)	0.8957	0.7564	1.394	0.5438	0.2741
	HSDT (Thai *et al*. 2013)	0.8984	0.7573	1.396	0.5442	0.2737
	Quasi-3D (Carrera *et al*. 2008)	0.9012	0.757	1.4147	0.5421	0.2496
	Quasi-3D (Wu *et al*. 2011)	0.9013	0.7571	1.4133	0.5436	0.2495
4	Present 11^2 node	1.0501	0.8823	1.1796	0.5668	0.2586
	SSDT (Zenkour 2006)	1.0941	0.8819	1.1783	0.5667	0.258
	HSDT (Nguyen 2015)	1.0466	0.8818	1.1766	0.5664	0.2593
	ITSDT (Kulkarni *et al*. 2015)	1.0469	0.882	1.1766	0.5664	0.2611
	TSDT (Wu *et al*. 2010)	1.0502	0.8815	1.1794	0.5669	0.2519
	HSDT (Mantari *et al*. 2012)	1.0457	0.8814	1.1755	0.5662	0.2623
	HSDT (Thai *et al*. 2013)	1.0502	0.8815	1.1794	0.5669	0.2537
	Quasi-3D (Carrera *et al*. 2008)	1.0541	0.8823	1.1985	0.5666	0.2362
	Quasi-3D (Wu *et al*. 2011)	1.0541	0.8823	1.1841	0.5671	0.2362
	Quasi-3D (Neves *et al*. 2012a)	-	0.875	1.1783	-	-
	Quasi-3D (Neves *et al*. 2012b)	-	0.9886	1.1593	-	-
	Quasi-3D (Neves *et al*. 2013)	-	0.9888	1.1588	-	-
	Quasi-3D (Carrera *et al*. 2011)	-	1.0072	1.1971	-	-
	HSDT (Belabed *et al*. 2014)	-	0.9812	1.146	-	-

	Present 11^2 node	1.0768	0.9747	0.9451	0.5882	0.2012
	SSDT (Zenkour 2006)	1.134	0.975	0.9466	0.5856	0.2121
	HSDT (Nguyen 2015)	1.0719	0.9744	0.9444	0.5852	0.2117
	ITSDT (Kulkarni *et al*. 2015)	1.0724	0.9747	0.9447	0.5853	0.2135
8	TSDT (Wu *et al*. 2010)	1.0763	0.9747	0.9477	0.5858	0.2087
	HSDT (Mantari *et al*. 2012)	1.0709	0.9737	0.9431	0.585	0.214
	HSDT (Thai *et al*. 2013)	1.0763	0.9746	0.9477	0.5858	0.2088
	Quasi-3D (Carrera *et al*. 2008)	1.083	0.9738	0.9687	0.5879	0.2262
	Quasi-3D (Wu *et al*. 2011)	1.083	0.9739	0.9622	0.5883	0.2261

nodes. In other words, the EFG method with an 11×11 node distribution reaches results comparable to the EMKI method with a 15×15 node distribution and the FEM method with more than 400 mesh points. Naturally, reducing the number of nodes decreases computation time. All simulations in this dissertation were performed using MATLAB 2016.

The graphic presentation of the numerical results reported in Table 2, is provided in Fig. 4. This figure demonstrates that the proposed method achieves excellent numerical accuracy and stability compared to FEM and EMKI. It reaches the converged value of $W^* \approx 4.618 \times 10^{-2}$ using fewer divisions, indicating superior computational efficiency. Furthermore, the method shows minimal sensitivity to node distribution, confirming its robustness and suitability for meshfree FGM plate analysis.

The following this section compares the flexural analysis results of the P-FGP (Al/Al_2O_3) plate using the EFG method with 11×11 nodes with other analytical methods available in previous references, as shown in Table 3 and Table 4. In this analysis, sinusoidal loading $q(x,y) = q_0 Sin\,\pi x/a\, Sin\,\pi x/b$is applied to the P-FGP. Table 3 presents a comparison between the first-order analysis, which suffers from shear locking in thin plates, and the third-order analysis along with other shear-locking-free references. The results demonstrate that the proposed third-order method maintains high accuracy even for thin plate analysis.

As observed in Table 3 and Table 4 and Figs. 5-7 with an increase in the ***n*** index, the effective elastic modulus $E_{eff}(z)$ of the P-FGP tends toward the metal's elastic modulus. Consequently, a reduction in the effective elastic modulus is observed, along with a decrease in the values of $\sigma^*_{xz}(z = h/6)$ and an increase in $W^*_{(z=0)}$. The reason for the increased error in the results of $\sigma^*_{xz}(z = h/6)$ compared to the three-dimensional solution is related to the inherent nature of HSDT. As mentioned by Nguyen in reference (Nguyen, 2015), in HSDT, the thickness stretching effect is considered approximately. This is also evident in other references listed in Table 3 and Table 4. Following this, the graphs of the variations of W^*, σ^*_{xx}, σ^*_{xy} and σ^*_{xz} along with the thickness of the thick functionally graded plate, are analyzed.

Fig. 5 shows the variations of σ^*_{xx} along the thickness. For a more detailed examination, magnifications are provided in areas where overlapping graphs occur (areas A, B, and C). As seen in the magnification of area A (refer to Fig. 5(b) for further details), when the ***n*** index approaches zero ($n = 0$), the effective elastic modulus E_{eff} tends toward absolute ceramic behavior, and the flexural behavior of the plate approaches homogeneous characteristics. In this case, based on the principles of strength of materials, the neutral axis passes through the center of the plate's surface, and as observed, there is symmetry in the compressive and tensile regions, and the stress variations are linear. With changes in the $n \geq 1$, it is observed that, along with the displacement of the neutral

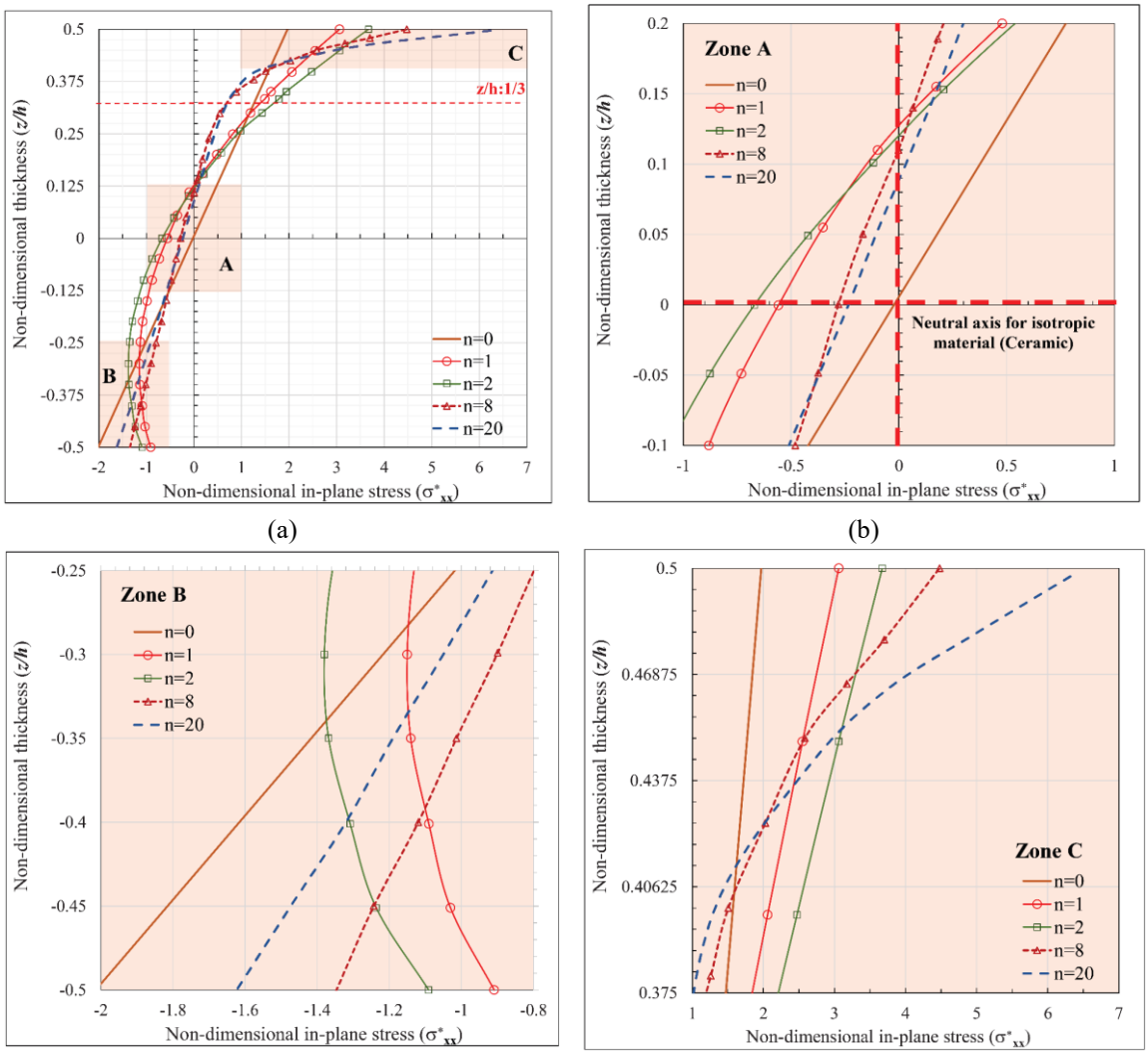

Fig. 5 (a) Variation of σ^*_{xx} along the thickness of the P-FGP(Al/Al2O3), (*a*/*h*=10) under sinusoidal loading, (b) Magnified view of region A, (c) Magnified view of region B and (d) Magnified view of region C.

axis position, the stress variations along the thickness become nonlinear. This is due to the parameter E_{eff}, which is influenced by z/h. Additionally, it is observed that with an increase in the $n \geq 1$, the position of the neutral axis returns toward the center of the surface, such that in the case of $n \to \infty$, E_{eff} tends toward absolute metallic behavior, and linear stress behavior reoccurs. As observed in the magnified view of region B (refer to Fig. 5(c) for further details), when $n \geq 1$, σ^*_{xx} increases at the position $z/h = -0.5$. Similarly, the magnified view of region C (refer to Fig. 5(d) for further details) shows that with an increase in the $n \geq 1$, σ^*_{xx}. Also, increases at the position $z/h = +0.5$. From comparing the graphs, it can be concluded that in every case, the maximum σ^*_{xx} occurs at the upper surface $z/h = +0.5$. Additionally, it is observed that in all plotted cases, σ^*_{xx} is

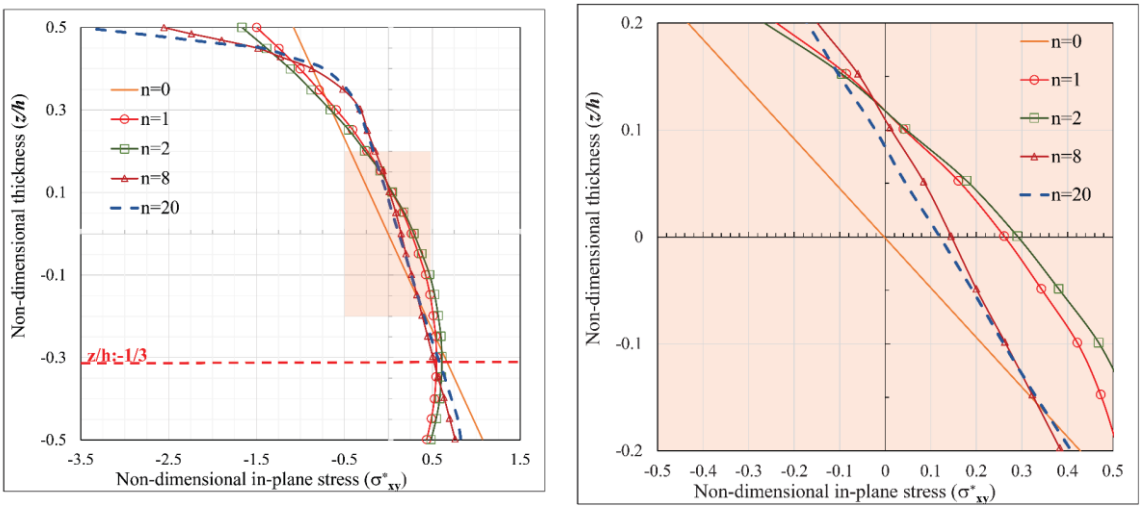

Fig. 6 (a) Variation of σ^*_{xy} along the thickness of the P-FGP(Al/Al_2O_3), (a/h=10) under sinusoidal loading and (b) Magnified view of region A

continuous, distinguishing it from ordinary composite and multilayered plates. A magnified view is provided in the region where the graph overlaps (shaded area) for a more detailed examination. As seen in the magnified view, when the ***n*** index approaches zero, the effective elastic modulus E_{eff} tends toward absolute ceramic behavior, and the flexural behavior of the plate approaches homogeneous characteristics. In this case, linear stress variations and symmetry in the upper and lower regions relative to the position $z/h = 0.00$ are observed. With changes in the $n \geq 1$, it is observed that the position of the neutral axis shifts, and the stress variations along the thickness become nonlinear.

The variations of σ^*_{xy} along the thickness are shown in Fig. 6. As observed, when ***n*** index increases ($n \geq 1$), σ^*_{xy} increases at the position $z/h = +0.5$. From comparing the graphs, it can be concluded that in every case, the maximum σ^*_{xy} occurs at the upper surface $z/h = +0.5$. It is also observed that the variations of σ^*_{xy} at the position $z/h = 0.00$ are negligible compared to the maximum value of σ^*_{xy}, and at the position $z/h = 0.333, \sigma^*_{xy}$ is almost equal to the homogeneous ceramic section. In other words, at this position, σ^*_{xy} is independent of the ***n*** index. The results shown in Table 3 also indicate this fact.

The variations of σ^*_{xz} along the thickness are shown in Fig. 7. As observed, when the ***n*** index approaches zero, the effective elastic modulus E_{eff} tends toward absolute ceramic behavior, and the flexural behavior of the plate approaches homogeneous characteristics. In this case, according to Timoshenko's theory and the principles of strength of materials, the shear stress variations are parabolic. With an increase in the ***n*** index, the behavior of σ^*_{xz} deviates from the parabolic shape, as shown in Fig. 7(a). It is also observed that the shear stress at the upper and lower surfaces $z/h = \pm 0.5$ is zero, which confirms the accuracy of the EFG method in implementing the HSDT theory in thick, functionally graded plates. In all plotted cases, σ^*_{xz} is continuous, which distinguishes it from ordinary composite and multilayered plates.

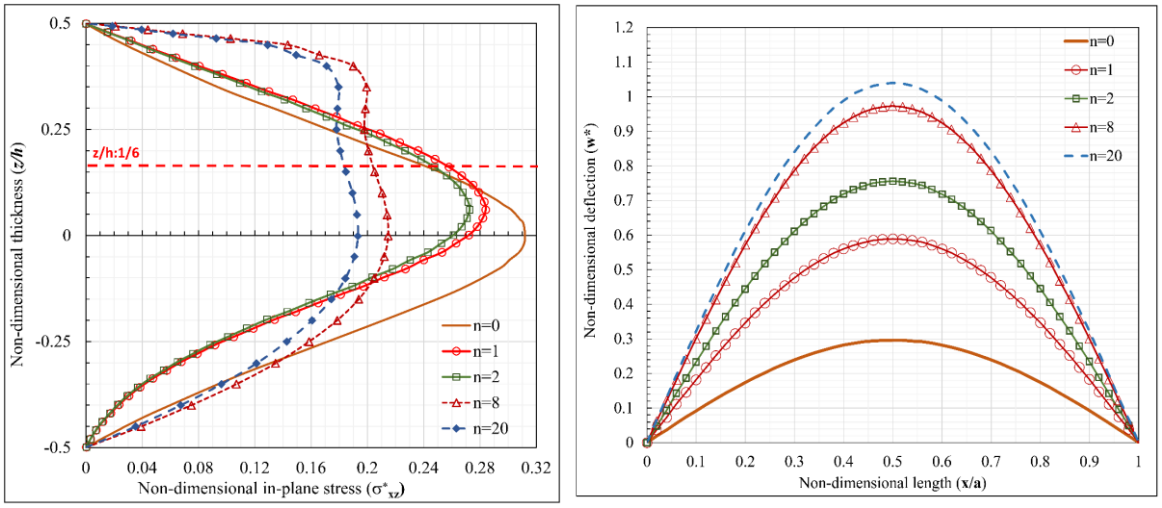

(a) (b)

Fig. 7 (a) Variation of σ^*_{xz} along the thickness of the P-FGP(Al/Al₂O₃), (*a*/*h*=10) under sinusoidal loading and (b) Variation of W^* along the thickness of the P-FGP(Al/Al₂O₃), (*a*/*h*=10) under sinusoidal loading

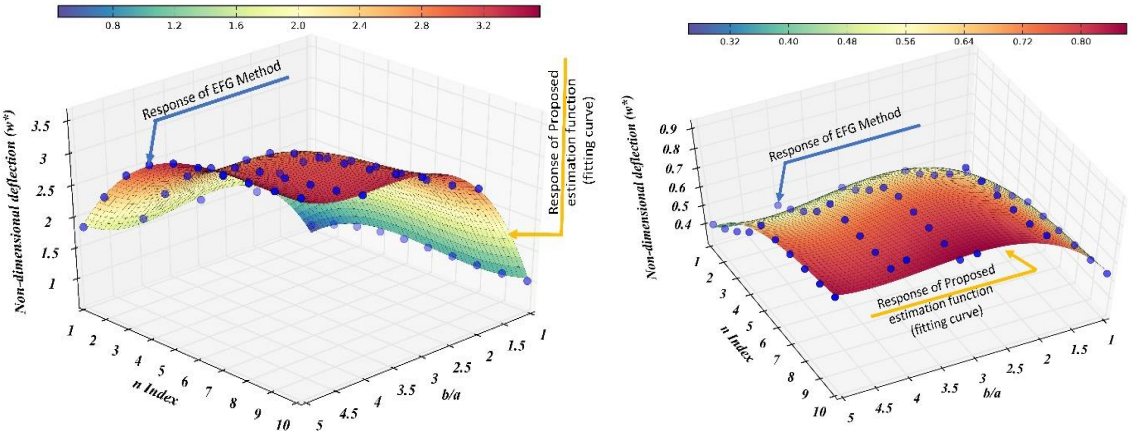

(a) *SSSS* (b) *SCSC*

Fig. 8 Fitting curve of estimation function for P-FGP (Al/Al₂O₃) for *a*/*h*=10 under sinusoidal loading

The variations of W^*along the dimensionless edge x/a as shown in Fig. 7(b). As observed, with an increase in the ***n*** index, W^* increases, which is due to the decrease in E_{eff} and the tendency toward metallic behavior of the section. The variations of W^* in the P-FGP fall within the range between ceramic-rich and metal-rich regions.

In this section of the paper introduces a novel three-dimensional estimation based on the sigmoid-cubic functions (Huang and He 2024, Sabir *et al*. 2024) and the findings of the EFG method. The function is presented for the estimation $W(a/2,b/2,0)$ of P-FGP (Al/Al₂O₃) with various boundary conditions and *b*/*a* ratio (*a*/*h*=5, 10) under sinusoidal lateral loading. The estimation function is presented in the following form:

Table 5 The constant coefficients of proposed estimation function of the rectangular P-FGP (Al/Al_2O_3) with sinusoidal loading

Coefficients	*a/h*	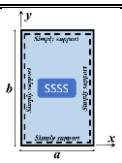 *SSSS*	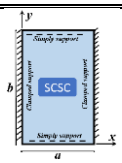 *SCSC*	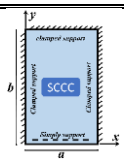 *SCCC*	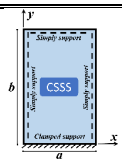 *CSSS*	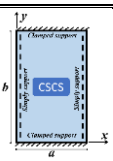 *CSCS*	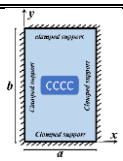 *CCCC*
H_1		3.36	3.292973	6.376619	1.585422	0.844493	0.833092
H_2		1.098254	0.706086	1.17463	1.240798	1.243257	1.243257
H_3		0.082768	0.580726	0.504175	-0.13195	-0.16042	-0.16042
H_4		-0.05193	-0.10679	-0.37709	-0.04627	-0.04013	-0.04013
H_5		-0.07765	-0.24435	-0.21514	0.01844	0.036178	0.036178
H_6		-0.0005	0.015904	0.063526	0.001759	0.001191	0.001191
H_7		0.011746	0.029538	0.026566	-0.00029	-0.00282	-0.00282
H_8	10	0.000318	-0.0008	-0.00332	6.59E-05	9.5E-05	9.5E-05
H_9		0.025315	0.015678	0.015309	0.015626	0.012954	0.012954
H_{10}		-0.00201	-0.00128	-0.00138	-0.00093	-0.00062	-0.00062
H_{11}		-0.00095	-0.0006	-0.0005	-0.00058	-0.00053	-0.00053
H_{12}		3.129707	3.908357	5.131611	3.329009	38.99569	5.49713
H_{13}		2.30181	2.419216	3.096622	3.264933	39.64313	5.316979
H_{14}		0.639537	0.600504	1.727304	0.520694	0.542397	0.566445
H_{15}		0.709911	0.50489	0.531209	0.45404	0.43406	0.440194
H_1		3.748667	3.650894	1.967149	2.00879	1.246997	1.210177
H_2		1.070796	0.601434	1.144806	1.262552	1.317377	1.253913
H_3		0.079351	0.538279	-0.06962	-0.17527	-0.21181	-0.19407
H_4		-0.03594	-0.00423	-0.02235	-0.03795	-0.05012	-0.03165
H_5		-0.07191	-0.22004	-0.00648	0.027432	0.037891	0.0408
H_6		-0.00251	-0.00419	-0.00407	-0.00388	-0.00331	-0.0047
H_7		0.010864	0.026247	0.002862	-0.00093	-0.00241	-0.00294
H_8	5	0.000417	0.000439	0.0005	0.000523	0.000539	0.000573
H_9		0.022182	0.009734	0.019782	0.02855	0.034154	0.028023
H_{10}		-0.00174	-0.00067	-0.00151	-0.0024	-0.00247	-0.00236
H_{11}		-0.00086	-0.00051	-0.00086	-0.00104	-0.0014	-0.00108
H_{12}		3.004349	3.39304	3.559445	3.107764	3.13317	4.118585
H_{13}		2.269255	2.185232	2.897584	3.041131	3.666277	4.000409
H_{14}		0.685417	0.702271	0.777499	0.758944	0.873293	0.847815
H_{15}		0.678493	0.675046	0.648494	0.646088	0.637777	0.627282

$$W(a/2,b/2,0)|0<n\leq 10,\Psi\leq 6=\left(\frac{H_1}{H_0}\right)\times\frac{H_2+H_3\Psi+H_4n+H_5\Psi^2+H_6n^2+H_7\Psi^3+H_8n^3+H_9\Psi n+H_{10}\Psi^2n+H_{11}\Psi n^2}{(1+exp(H_{12}-H_{13}\Psi))(1+exp(H_{14}-H_{15}n))} \quad (48)$$

where $\{H_i i = 1,2,..,15\}$ are the constant coefficients, $\Psi = b/a$ and $\boldsymbol{n}$ is power index. The H_0 coefficient represents the dimensionless factor, which is equal to $10E_c h^3/q_0 a^4$ in this example. Table 5 reports the constant coefficients $\{H_i i = 1,2,..,15\}$ of proposed estimation function of the thick rectangular P-FGP (Al/Al_2O_3) with sinusoidal loading. Also, in order to demonstrate the precision of the proposed methodology, the convergence of the P-FGP (Al/Al_2O_3) with the characteristics (*SSSS*, *SCSC a/h*=10) is illustrated in Fig. 8. As can be observed, the proposed estimation function demonstrates a high degree of convergence to the EFG response. The maximum error of the estimation function $\mathrm{Erorr}(\%)$ is 4.83%

6. Conclusions

In this study, The EFG method was employed for the static bending analysis of thick P-FGPs. In order to model the shear strains and the thickness stretching effect on the static bending behavior of thick FGPs, the Reddy's higher-order shear deformation theory (HSDT) was employed. In the proposed method has accurately satisfied the continuity condition C^1 of the displacement field. To eliminate the shear-locking challenge, the derivative of the deflection shape function has been used for the interpolation of rotation. It was shown in thick P-FGPs, an increase in the n index leads to the convergence of the effective elastic coefficient with respect to the metal. As a result, transverse stresses and displacements increase. Additionally, it was demonstrated that the discrepancy between the outcomes and the 3D solution could be attributed to the intrinsic characteristics of HSDT. As previously pointed out by Nguyen *et al*. (2016), in HSDT, the effect of thickness stretching is approximately taken into account. Furthermore, the effect of various factors, including the two-phase feature of functionally graded material (FGM), aspect ratio and length-to-thickness ratio, on the displacements and stresses of thick P-FGM plates was investigated. Finally, new three-dimensional estimation functions was proposed to determine the center deflection of P-FGPs which is based on the combination of interpolation functions (sigmoid-cubic) and EFG response. A comparative analysis of the estimation function results reveals that the proposed estimation function represents a robust methodology for characterizing the response curve and offers an insightful analysis into the static bending behavior in thick FG plates. Moreover, the results of this approach demonstrate that the estimation functions can be highly efficient, offering a significant advancement in the analysis of such structures.

References

Amiri, A., Rahmani, H. and Ahmadi Balootaki, M. (2020), "Torsional wave propagation in 1D and two dimensional functionally graded rod", *J. Comput. Appl. Mech.*, **51**(1), 1-21. https://doi.org/10.22059/jcamech.2019.272234.350

Belabed, Z., Houari, M.S.A., Tounsi, A., Mahmoud, S.R. and Bég, O.A. (2014), "An efficient and simple higher order shear and normal deformation theory for functionally graded material (FGM) plates", *Compos. Part B Eng.*, **60**, 274-283. https://doi.org/10.1016/j.compositesb.2013.12.057

Belarbi, H., Boucham, B., Bourada, F., Kaci, A., Bourada, M. and Tounsi, A. (2024), "Investigation on thermomechanical bending of functionally graded sandwich plates using a novel combined 2d integral plate model", *Phys. Mesomech.*, **27**(4), 472-484. https://doi.org/10.1134/S1029959924040118

Benmalek, H., Bouziane, S., Bouzerd, H. and Suleiman, H. (2024), "Innovative mixed finite element method for bending analysis of functionally graded beams: modelling, validation, and applications", *Eng. Res. Exp.*,

6(1), 015055. https://doi.org/10.1088/2631-8695/ad1f16

Chakraborty, A., Gopalakrishnan, S. and Reddy, J. (2003), "A new beam finite element for the analysis of functionally graded materials", *Int. J. Mech. Sci.*, **45**(3), 519-539. https://doi.org/10.1016/S0020-7403(03)00058-4

Dai, K.Y., Liu, G.R., Lim, K.M., Han, X. and Du, S.Y. (2004), "A meshfree radial point interpolation method for analysis of functionally graded material (FGM) plates", *Comput. Mech.*, **34**, 213-223. https://doi.org/10.1007/s00466-004-0566-0

Ghadiri Rad, M. H., Shahabian, F. and Hosseini, S.M. (2015), "A meshless local Petrov–Galerkin method for nonlinear dynamic analyses of hyper-elastic FG thick hollow cylinder with Rayleigh damping", *Acta Mechanica*, **226**, 1497-1513. https://doi.org/10.1007/s00707-014-1266-2

Gu, Y.T. and Liu, G.R. (2001), "Using radial function basis in a boundary-type meshless method, boundary point interpolation method (BPIM)", *Int. Conf. Sci. Engr. Comput*, **1**, 68-75. https://doi.org/10.1016/B978-008043944-0/50973-2

Houari, M.S.A., Bessaim, A., Bezzina, S., Tounsi, A., Daikh, A.A., Garg, A. and Belarbi, M.O. (2024), "Thermoelastic bending analysis of thick functionally graded sandwich plates with arbitrary graded material properties using a novel quasi-3D HSDT", *Arch. Civil Mech. Eng.*, **24**(2), 80-90. https://doi.org/10.1007/s43452-024-00898-6

Huang, H.H. and He, Q. (2024), "Nonlinear regression analysis", *arXiv preprint arXiv*, 2402.05342.

Keleshteri, M.M. and Jelovica, J.J.E.S. (2022), "Analytical solution for vibration and buckling of cylindrical sandwich panels with improved FG metal foam core", *Eng. Struct.*, **266**, 114580. https://doi.org/10.48550/arXiv.2402.05342

Khalfi, H., Naciri, I., Raghib, R., Randrianarivelo, J., Yu, J., Ratolojanahary, F.E. and Elmaimouni, L. (2024), "Axisymmetric free vibration modeling of a functionally graded piezoelectric resonator by a double Legendre polynomial method", *Acta Mechanica*, **235**(2), 615-631. https://doi.org/10.1007/s00707-023-03766-1

Konda, D.H., Santiago, J.A.F., Telles, J.C.F., Mello, J.P.F. and Costa, E.G.A. (2019), "A meshless Reissner plate bending procedure using local radial point interpolation with an efficient integration scheme.", *Eng. Anal. Bound. Elem.*, **99**, 46-59. https://doi.org/10.1016/j.enganabound.2018.11.004

Kulkarni, K., Singh, B.N. and Maiti, D.K. (2015), "Analytical solution for bending and buckling analysis of functionally graded plates using inverse trigonometric shear deformation theory", *Compos. Struct.*, **134**, 147-157. https://doi.org/10.1016/j.compstruct.2015.08.060

Li, J., Pokkalla, D.K., Wang, Z.P. and Wang, Y. (2023), "Deep learning-enhanced design for functionally graded auxetic lattices", *Eng. Struct.*, **292**, 116477. https://doi.org/10.1016/j.engstruct.2023.116477

Li, S.R., Zhang, F. and Liu, R.G. (2024), "Classical and homogenized expressions for the bending solutions of FGM plates based on the four variable plate theories", *Mech. Adv. Mater. Struct.*, **31**(15), 3413-3424. https://doi.org/10.1155/2020/2836763

Liu, G.R. (2009), *Moving Beyond the Finite Element Method*, CRC Press, Florida.

Mantari, J.L., Oktem, A.S. and Soares, C.G. (2012), "Bending response of functionally graded plates by using a new higher order shear deformation theory", *Compos. Struct.*, **94**(2), 714-723. https://doi.org/10.1016/j.compstruct.2011.09.007

Martínez-Pañeda, E. (2019), "On the finite element implementation of functionally graded materials", *Materials*, **12**(2), 287. https://doi.org/10.3390/ma12020287

Neves, A.M.A., Ferreira, A.J.M., Carrera, E., Cinefra, M., Roque, C.M.C., Jorge, R.M.N. and Soares, C.M.M. (2012b), "A quasi-3D hyperbolic shear deformation theory for the static and free vibration analysis of functionally graded plates", *Compos. Struct.*, **94**(5), 1814-1825. https://doi.org/10.1016/j.compstruct.2011.12.005

Neves, A.M.A., Ferreira, A.J.M., Carrera, E., Cinefra, M., Roque, C.M.C., Jorge, R.M.N. and Soares, C.M.M. (2013), "Static, free vibration and buckling analysis of functionally graded plates using a quasi-3D higher-order shear deformation theory and a meshless technique", *Compos. Struct.*, **44**, 657-674. https://doi.org/10.1016/j.compositesb.2012.01.089

Neves, A.M.A., Ferreira, A.J.M., Carrera, E., Roque, C.M.C., Cinefra, M., Jorge, R.M.N. and Soares, C.M.M.

(2012a), "A quasi-3D sinusoidal shear deformation theory for the static and free vibration analysis of functionally graded plates", *Compos. Part B Eng.*, **43**(2), 711-725. https://doi.org/10.1016/j.compositesb.2011.08.009

Nguyen, T.K. (2015), "A higher-order hyperbolic shear deformation plate model for analysis of functionally graded materials", *Int. J. Mech. Mater. Des.*, **11**, 203-219. https://doi.org/10.1007/s10999-014-9260-3

Nguyen, T.K., Nguyen, V.H., Chau-Dinh, T., Vo, T.P. and Nguyen-Xuan, H. (2016), "Static and vibration analysis of isotropic and functionally graded sandwich plates using an edge-based MITC3 finite elements", *Compos. Part B Eng.*, **107**, 162-173. https://doi.org/10.1007/s11709-022-0891-4

Nguyen, T.K., Sab, K. and Bonnet, G. (2008), "First-order shear deformation plate models for functionally graded materials", *Compos. Struct.*, **83**(1), 25-36. https://doi.org/10.1016/j.compstruct.2007.03.004

Pham, Q.H., Tran, T.T., Zenkour, A.M. and Nguyen-Thoi, T. (2023), "Multi-objective optimization for free vibration of L-shaped bi-functionally graded sandwich plates using an effective finite element method and non-dominated sorting genetic algorithm II", *Compos. Struct.*, **326**, 117622. https://doi.org/10.1016/j.compstruct.2023.117622

Rad, M.H.G., Shahabian, F. and Hosseini, S.M. (2020), "Geometrically nonlinear dynamic analysis of FG graphene platelets-reinforced nanocomposite cylinder: MLPG method based on a modified nonlinear micromechanical model", *Steel Compos. Struct.*, **35**(1), 77-92. https://doi.org/10.12989/scs.2020.35.1.077.

Reddy, J. (2000), "Analysis of functionally graded plates", *Int. J. Numer. Meth. Eng.*, **47**(1-3), 663-684. https://doi.org/10.1002/(SICI)1097-0207(20000110/30)47:1/3<663::AID-NME787>3.0.CO,2-8

Sabir, Z., Dirani, S., Bou Saleh, S., Mabsout, M.K. and Arbi, A. (2024), "A novel radial basis and sigmoid neural network combination to solve the human immunodeficiency virus system in cancer patients", *Mathematics*, **12**(16), 2490. https://doi.org/10.3390/math12162490

Singh, S.P., Rohith, R.P., Nirmal, S.F., Raja, D.E. and Ravichandran, P. (2024), "Improvement in manufacturing of aluminum-based functionally graded materials through centrifugal casting—A review", *Eng. Proc.*, **61**(1), 16. https://doi.org/10.3390/engproc2024061016

Slimani, R., Menasria, A., Ali Rachedi, M., Mourad, C., Refrafi, S. and Nimer, A.A. (2024), "A novel quasi-3D refined HSDT for static bending analysis of porous functionally graded Plates", *J. Comput. Appl. Mech.*, **1**, 50-59. https://doi.org/10.22059/JCAMECH.2024.372417.968

Slimani, R., Menasria, A., Ali Rachedi, M., Mourad, C., Refrafi, S., Nimer, A.A. and Mamen, B. (2024), "A novel quasi-3D refined HSDT for static bending analysis of porous functionally graded Plates", *J. Comput. Appl. Mech.*, **55**(3), 519-537. https://doi.org/10.22059/jcamech.2024.372417.968

Swami, S.K. and Ghugal, Y.M. (2021), "Thermoelastic bending analysis of laminated plates subjected to linear and nonlinear thermal loads", *Adv. Aircr. Spacecr. Sci.*, **8**(3), 213-237. https://doi.org/10.12989/aas.2021.8.3.213

Taczała, M., Buczkowski, R. and Kleiber, M. (2022), "Analysis of FGM plates based on physical neutral surface using general third-order plate theory", *Compos. Struct.*, **301**, 116218. https://doi.org/10.1016/j.compstruct.2022.116218

Thai, H.T. and Kim, S.E. (2013), "A simple higher-order shear deformation theory for bending and free vibration analysis of functionally graded plates", *Compos. Struct.*, **96**, 165-173. https://doi.org/10.1016/j.compstruct.2012.08.025

Thang, P.T., Kim, C. and Kim, J. (2023), "Free vibration analysis of bi-directional functionally graded cylindrical shells with varying thickness", *Aerosp. Sci. Tech.*, **137**, 108271. https://doi.org/10.1016/j.ast.2023.108271

Vakili, S.A., Shahabian, F. and Ghadiri Rad, M.H. (2021), "Analyzing of thick plates with cutouts using the meshless (EFG) method based on higher order shear deformation theories for solving shear-locking issue", *Numer. Meth. Civil Eng.*, **5**(4), 46-59. https://doi.org/10.52547/nmce.5.4.46

Vakili, S.E., Homami, P. and Esfahani, M.R. (2019), "Effect of fibers and hybrid fibers on the shear strength of lightweight concrete beams reinforced with GFRP bars", *Structures*, **20**, 290-297. https://doi.org/10.1016/j.istruc.2019.04.006

Van Vinh, P., Avcar, M., Belarbi, M.O. and Tounsi, A. (2023), "A new higher-order mixed four-node quadrilateral finite element for static bending analysis of functionally graded plates", *Structures*, **47**, 1595-

1612. https://doi.org/10.1016/j.istruc.2022.11.113
Vel, S.S. and Batra, R.C. (2002), "Exact solution for thermoelastic deformations of functionally graded thick rectangular plates", *AIAA J.*, **40**(7), 1421-1433. https://doi.org/10.2514/3.15212
Wu, C.P. and Chiu, K.H. (2011), "RMVT-based meshless collocation and element-free Galerkin methods for the quasi-3D free vibration analysis of multilayered composite and FGM plates", *Compos. Struct.*, **93**(5), 1433-1448. https://doi.org/10.1016/j.compositesb.2011.03.013
Wu, C.P. and Li, H.Y. (2010), "An RMVT-based third-order shear deformation theory of multilayered functionally graded material plates", *Compos. Struct.*, **92**(10), 2591-2605. https://doi.org/10.1016/j.compstruct.2010.01.022
Zenkour, A.M. (2006), "Generalized shear deformation theory for bending analysis of functionally graded plates", *Appl. Math. Modell.*, **30**(1), 67-84. https://doi.org/10.1016/j.apm.2005.03.009

CC